High resolution near-IR spectroscopy of FGK stars

Daniel Thaagaard Andreasen

April 12, 2017

CONTENTS

Contents i

Abstracts iii

List of Figures iv

List of Tables v

1 Introduction 1
- 1.1 Exoplanets 3
- 1.2 Planet host stars 3
- 1.3 This thesis 3

2 Theory 5
- 2.1 Stellar structure 5
- 2.2 Stellar atmosphere 7
  - 2.2.1 Atmosphere models 10
  - 2.2.2 Radiative transfer code - MOOG 10
  - 2.2.3 The equivalent width 11
    - 2.2.3.1 Temperature dependence 12
    - 2.2.3.2 Pressure dependence 12
    - 2.2.3.3 Abundance dependence 15
    - 2.2.3.4 Microturbulence 16
- 2.3 Line list and atomic data 17
- 2.4 Spectrographs 18

3 Deriving stellar parameters 21
- 3.1 Methods for deriving stellar atmospheric parameters 21
  - 3.1.1 InfraRed Flux Method - IRFM 21
  - 3.1.2 Photometry 22
  - 3.1.3 Spectroscopy 22
- 3.2 Other stellar parameters 22
  - 3.2.1 Asteroseismology 22

3.3 `FASMA` 22
  3.3.1 Ingredients 22
  3.3.2 Wrapper for `ARES` 23
  3.3.3 Interpolation of atmosphere models 24
  3.3.4 Minimization 24
  3.3.5 Error estimate 28

4 Results for FGK stars **31**
4.1 HD20010 31
4.2 Arcturus 31
4.3 10 Leo 31
4.4 Synthetic cool stars 31

5 Future work **33**

Bibliography **35**

ABSTRACTS

LIST OF FIGURES

2.1 Energy levels for hydrogen, $E_n = \frac{-13.6\,\mathrm{eV}}{n^2}$. 9
2.2 An absorption line centred at λ_0 normalised at the flux level F_c. The area of the absorption line to the left is equal to the blue shaded area in the rectangle to the right with width EW. 11
2.3 The EW for a Fe I and Fe II line with increasing T_{eff}. The two lines have similar EW in the Sun and are found in the optical part of the spectrum. 13
2.4 *Upper panel*: Curve of growth for same Fe II used in Figure 2.3 for four different $\log g$ values. Here it is the weak lines mostly affected by the change in $\log g$. *Lower left panel*: Synthetic spectra of the same line. The colour scale is the same. *Lower right*: The abundance for the line at different $\log g$. A strong correlation (0.40) is seen. . 15
2.5 *Upper panel:* Curve of growth of the same Fe I line as used in Figure 2.3. Four points are marked which is shown in the *lower panel* as a synthetic spectral line. The RW (proxy for EW) is clearly increasing with $\log gf$ (proxy for abundance). 16
2.6 Curve of growth for three different values of ξ_{micro}. The EW is increasing with increasing ξ_{micro}. 17

3.1 Model atmosphere grid from Kurucz (1993) at [Fe /H] = 0.00 between 3000 K and 10 000 K. The grid extends to higher T_{eff}, but these are not considered in this thesis. 25
3.2 The abundances of Fe I for the planet host star: HATS-1. Upper plot: Converged parameters (see text for stellar parameters for this star). Middle plot: Converged parameters with 0.5 km/s added to ξ_{micro}. Lower plot: Converged parameters with 500 K added to T_{eff}. 27
3.3 Overview of the minimization for `FASMA` . Credit: Andreasen et al. (2017a). 29

LIST OF TABLES

CHAPTER 1

INTRODUCTION

Effective temperature ($T_{\rm eff}$), surface gravity ($\log g$), and metallicity ([M/H], where iron is normally used as a proxy) are fundamental atmospheric parameters necessary to characterise a single star, and to determine other indirectly fundamental parameters such as mass, radius, and age from stellar evolution models (see e.g. Baraffe et al., 2015; Dotter et al., 2008; Girardi et al., 2000). Precise and accurate stellar parameters are also essential in exoplanet searches. Planetary radius and mass are mainly found from transit lightcurve analysis and radial velocity analysis, respectively. The determination of the mass of the planet implies a knowledge of the stellar mass, while the measurement of the radius of the planet is dependent on our capability to derive the radius of the star (see e.g. Ammler-von Eiff et al., 2009; Torres et al., 2012, 2008).

The derivation of precise stellar atmospheric parameters is not a simple task. Different approaches often lead to discrepant results (see e.g. Lebzelter et al., 2012; Santos et al., 2013; Torres et al., 2010). Interferometry is usually considered an accurate method for deriving stellar radii (see e.g. Boyajian et al., 2012); however, it is only applicable for bright nearby stars. Asteroseismology, on the other hand, reveals the inner stellar structure by observing the stellar pulsations at the surface. From asteroseismology it is possible to measure the surface gravity and mean density, and therefore to calculate mass and radius with high precision (see e.g. Kjeldsen and Bedding, 1995). However, for stars on the main sequence asteroseismic methods can typically only be applied to FG stars, since the oscillation modes of K and M dwarfs are likely too weak to be detected even with high precision spectroscopy or photometry. Moreover, the effective temperature is needed when applying asteroseismology in order to obtain the surface gravity and the mean density.

A crucial parameter for the indirect determination of stellar bulk properties is the T_{eff}. In that respect, the infrared flux method (IRFM) has proven to be reliable for FGK dwarf and subgiant stars. For higher accuracy the IRFM needs a priori knowledge of the bolometric flux, reddening, surface gravity, and stellar metallicity (Blackwell and Shallis, 1977; Casagrande et al., 2010; Ramírez and Meléndez, 2005).

Finally, the use of high resolution spectroscopy along with stellar atmospheric models is an extensively tested method that allows the derivation of the fundamental parameters of a star (see e.g. Santos et al., 2013; Valenti and Fischer, 2005). The procedure depends on the quality of the spectra, their resolution, and wavelength region. A fit to the overall spectrum can be applied for all spectral resolutions, but are often time consuming (see e.g. Recio-Blanco et al., 2006; Tsantaki et al., 2014). For resolutions higher than $\lambda/\Delta\lambda \sim 20\,000$ we can apply the equivalent width (EW) method (see e.g. Andreasen et al., 2017a; Tsantaki et al., 2013, for details). However, while the latter approach is often faster than the synthetic fitting, it requires higher quality spectra, and the star to be slow rotating (below 10 km/s to 15 km/s).

Standard procedures are often used to derive stellar atmospheric parameters from high quality spectra in the optical (see e.g. Sousa et al., 2008; Valenti and Fischer, 2005). With the advancement of high resolution near-infrared (NIR) instruments, we will now be able to use a similar technique to that used in the optical part of the spectrum (see e.g. Bensby et al., 2014; Meléndez and Barbuy, 1999; Mucciarelli et al., 2013; Sousa et al., 2008; Tsantaki et al., 2013). At the moment, the GIANO spectrograph installed at *Telescopio Nazionale Galileo* (TNG) is already available (Origlia et al., 2014), as is the *infrared Doppler instrument* (IRD) installed at the Subaru telescope (Kotani et al., 2014), *Calar Alto high-Resolution search for M dwarfs with Exoearths with Near-infrared and optical Échelle Spectrographs* (CARMENES) for the 3.5 m telescope at Calar Alto Observatory (Quirrenbach et al., 2014), and iShell at the *InfraRed Telescope Facility* (Rayner et al., 2012, 2016). Three new spectrographs are planned for the near future: 1) The *CRyogenic InfraRed Echelle Spectrograph Upgrade Project* (CRIRES+) at the *Very Large Telescope* (VLT) (Follert et al., 2014) with expected first light in 2017, 2) *un SpectroPolarimètre Infra-Rouge A Near-InfraRed Spectropolarimeter* (SPIRou) at *The Canada-France-Hawaii Telescope* (CFHT) (Artigau et al., 2014; Delfosse et al., 2013) with expected first light in 2017 as well, and 3) *Near Infrared Planet Searcher* NIRPS at the ESO 3.6m telescope in La Silla (Conod et al., 2016). The spectral resolutions for these spectrographs range between 50 000 and 100 000.

With the advance of the next generation NIR spectrographs, we are still preparing the data analysis of stellar spectra, in particular how to get reliable atmospheric parameters (see e.g. Andreasen et al., 2016; Lindgren et al., 2016; Önehag et al., 2012). The analysis of stellar spectra is well understood for FGK stars in the optical part of the spectrum, however some work still needs to be done for the NIR part.

We continue our series of studies to explore the use of the NIR domain to derive stellar parameters for FGK and M stars. In particular, here we analyse the atlas of Arcturus and the spectrum of 10 Leo. For the analysis we use the iron line list presented in Andreasen et al. (2016) (referred to as Paper I). In Paper I we successfully tested our method on a slightly hotter star than the Sun, while in this work we aim to test the method on cooler stars. The strength of the NIR domain over the optical becomes clear when we move towards the cooler stars. Here we see less continuum depression and line blending due to in particular molecular features. Moreover, the cooler stars emit more light in the NIR domain than the optical, and with the lightest stars being intrinsically faint, we thus obtain the majority of the flux here.

1.1 Exoplanets

1.2 Planet host stars

With the present diversity of exoplanets it becomes increasingly important to get an accurate and precise characterisation of the planets in order to study them in samples and on an individual level. An accurate and precise characterisation can give us an idea whether the planet is rocky, composed of water or gaseous.

1.3 This thesis

CHAPTER 2

THEORY

To encompass all theory regarding stellar structure, evolution, and their atmosphere is far beyond the scope of this thesis. Rather the theory needed is presented below with highlights on the most important aspects.

2.1 Stellar structure

The structure of a non-rotating spherical stars can be described by five rather simple differential equations (see e.g. Kippenhahn and Weigert, 1994) presented below:

1. **Equation of Continuity**

   Relation between the mass, m, the density, ρ, at a symmetric shell at radius r

   $$\boxed{\frac{\partial r}{\partial m} = \frac{1}{4\pi r^2 \rho}.} \tag{2.1}$$

2. **Equation of Hydrostatic Equilibrium**

   The equation of hydrostatic equilibrium shows how a star in equilibrium is balanced between two forces. The inward force from gravity and the outward force from pressure, P,

   $$\boxed{\frac{\partial P}{\partial m} = -\frac{Gm}{4\pi r^4}.} \tag{2.2}$$

When working with asteroseismology a time dependent perturbation to this equation is added (see e.g. Aerts et al., 2010, for a thorough discussion). However, this term is neglected here.

3. **Equation of Energy Conservation**

   The equation of energy conservation shows how the energy is produced and lost throughout the star.

   $$\boxed{\frac{\partial l}{\partial m} = \varepsilon - \varepsilon_\nu + \varepsilon_g,} \tag{2.3}$$

   where ε is the energy production in the centre of the star, ε_ν is the energy lost by neutrinos which is always positive, ε_g is a source function of time-dependent terms, and l is the luminosity at m. ε_g comes from the fact that non-stationary shells can change its internal energy, and thus exchange mechanical energy with neighbouring shells.

4. **Equation of Energy Transport**

   Energy transportation throughout the star is described with the following equation

   $$\boxed{\frac{\partial T}{\partial m} = -\frac{GmT}{4\pi r^4 P}\nabla_{\mathrm{rad}},} \tag{2.4}$$

   where ∇_{rad} is the radiative temperature gradient, and T is the temperature. The value of the temperature gradient compared to the radiative temperature gradient tells if the energy is transported by convection or radiation. In our Sun the outer layer are convective while the inner layer are radiative.

5. **Equation of Chemical Composition**

   In this last equation we see the evolution of an element, X_i, when it reacts with other elements with reaction rates r_{ji} and r_{ik}

   $$\boxed{\frac{\partial X_i}{\partial t} = \frac{m_i}{\rho}\left(\sum_j r_{ji} - \sum_k r_{ik}\right).} \tag{2.5}$$

   Note that this is the only time-dependent equation of the five presented.

These five fundamental equations are implemented in stellar evolutionary codes, which we will use in later chapters. The many different codes that exist take other things into account, e.g the star can rotate, and it may not always be in hydrostatic equilibrium (this is important if we want our star to pulsate). For simplicity we have only presented time-dependence in the Equation of Chemical Composition since timescales of rotation, pulsations, and activity are much shorter than the long timescale found in chemical composition changes.

2.2 Stellar atmosphere

Much of this Section is inspired by Gray (2005). While all the figures here were made by the author of this thesis, most of them can be found in Gray (2005) as well.

Stellar atmospheres are rather complicated. This is where the light produced in the interior of the stars are released. However, the atmosphere of a star is not transparent to all light, and some of the light is absorbed in the atmosphere and later emitted in a random direction. The different elements in the atmosphere is the reason for absorbing light at specific wavelength. The strength of the absorption depends on the physical conditions in the atmosphere, the effective temperature (T_{eff}), the pressure/gravity ($\log g$), the overall metallicity ([Fe /H]), the specific abundance of a given element if different from the overall metallicity (A), and the atomic characteristics of the transition coursing the absorption line.

It is important to know the fraction of atoms excited to the nth energy level, N_n. This fraction is proportional to the statistical weight g_n and the Boltzmann factor and is described as:

$$\boxed{\frac{N_n}{N} = \frac{g_n}{u(T)} 10^{-\theta \chi_n}} \qquad \text{Boltzmann}$$

This equation is also called the Boltzmann equation. Here N is the total number of atoms per unit volume, $u(T) = \Sigma g_i e^{-\chi_i/kT}$ is the partition function, k is Boltzmann's constant, T is the temperature, and χ_n is the excitation potential for the lower energy level.

While atoms can get excited following Boltzmann's equation above, they can also get ionized. The ionization ratio for a collision dominated gas (which is a good approximation for FGKM stars) is described by the Saha equation. This equation relate the ratio of atoms in state r to atoms in the excited state above for the same element, $r + 1$, in the following way:

$$\boxed{\frac{N_{r+1}}{N_r} = \frac{1}{P_e} \frac{(2\pi m_e)^{3/2}(kT)^{5/2}}{h^3} \frac{2u_{r+1}(T)}{u_r(T)} e^{-I/kT} = \frac{\Phi(T)}{P_e}} \qquad \text{Saha}$$

here m_e is the electron mass, h is Planck's constant, I is the ionization potential of the neutral atom, and $\Phi(T)$ is all not related to the electron pressure, P_e.

The atomic lines are characterised by few quantum mechanical descriptors.

- The wavelength describes between which energy levels there is a transition, i.e. at which wavelength the light is absorbed.
- The ionization state, i.e. is it a atom element absorbing or a ionized atom.
- The excitation potential. This gives an idea how deep in the atmosphere a line is formed. If χ is high, then higher temperatures (i.e. higher random motion and more collisions between the atoms) is required for forming the absorption line. These higher temperatures are found deeper in the atmosphere.
- The oscillator strength, $\log gf$, is related to the atomic transition probability.
- The damping coefficients, is a natural damping (also known as radiation damping) caused by the uncertainty of lifetime in an energy level according to Heisenberg's uncertainty principle. This is related to a uncertainty in the energy level and thus a natural broadening is introduced.

These are essential to know from either theoretical calculations or experiments. The oscillator strength is a quantity that is difficult to measure, and this is often changed when absorption lines are matched with real observations of e.g. the Sun. This is a way of calibrating a line list and will be described in detail in Section 2.3.

It is important to mention that one of the main differences between absorption lines in optical and near-infrared is the excitation potential. The energy levels of an atom gets denser packed as the energy level increase as shown in Figure 2.1 for hydrogen. For hydrogen the energy levels E_n follow the very simple formula from Bohr's atomic model, $E_n = \frac{-13.6\,\mathrm{eV}}{n^2}$, where n is the principal quantum number, and 13.6 eV is the ionization energy for hydrogen, i.e. the minimum amount of energy required to ionize hydrogen. The energy levels for heavier atoms show a similar structure. The outer electron for a multi-electron atom is partially shielded from the nucleus by the inner electrons, and thus does not experience the full charge Z but rather an effective charge Z_{eff}, giving the expression

$$E_n = -hcR_\infty \frac{Z_{\mathrm{eff}}^2}{n^2}, \tag{2.6}$$

where h is Planck's constant, c is the speed of light, and R_∞ is Rydberg's constant.

With increasing n the energy levels get closer, or in other words the photon required to excite an electron from one energy level to a neighbouring state will get redder. These redder photons used for exciting an atom are the absorption lines seen in the NIR. However, the excitation to the lower state is from thermal motion and not coursed by photons. Since tight energy levels require a highly excited lower state, the temperature required here are similar high, which means that the NIR lines are typically formed in the deeper layers of the atmosphere compared to absorption lines seen in the optical part of the spectrum.

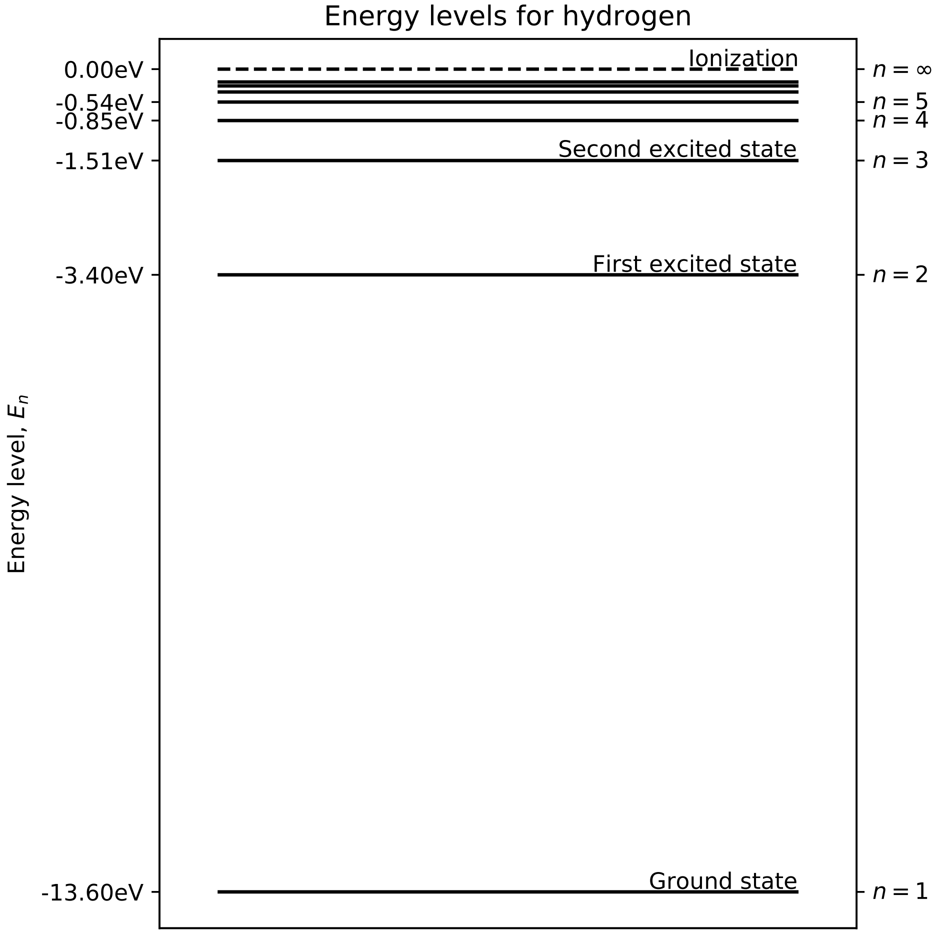
Energy levels for hydrogen
Energy level, E_n
0.00eV
-0.54eV
-0.85eV
-1.51eV
-3.40eV
-13.60eV
Ionization
Second excited state
First excited state
Ground state
$n = \infty$
$n = 5$
$n = 4$
$n = 3$
$n = 2$
$n = 1$

Figure 2.1: *Energy levels for hydrogen,* $E_n = \frac{-13.6\,\mathrm{eV}}{n^2}$.

The above discussed energy transitions are purely electronic, however there exists so called fine structure transitions as well. This is due to the spin of the electron (or magnetic moment) interacting with the orbital angular momentum of the electron. This leads to a splitting of the absorption line. In atoms there also exists an even finer structure, commonly known as the hyperfine structure. This structure arise due to the interaction between the magnetic field created by the electrons and the nuclear spin. These splittings are important to consider for some transitions and some atoms. For Fe the hyperfine structure is not important since the net nuclear spin (of protons) is 0 because there is an even number, hence hyperfine structure is only important for atoms with an odd number of protons. There are other splitting and shift for spectral absorption lines like the Zeeman splitting coursed by an external magnetic field, and the Stark effect splitting a line due to an external electric field. These two last effect are minor and will not be discussed more, however it is worth noting that the Zeeman splitting can be used to measure the strength of a magnetic field in a star if this is strong enough.

2.2.1 Atmosphere models

In order to derive abundances or calculate a synthetic spectrum, two main things are needed: 1) And atmosphere model, and 2) a radiative transfer code that solves the equations above. There are different atmosphere models available. Throughout this thesis the ATLAS9 model atmosphere are used by Kurucz (1993). Other mention-able atmosphere models includes MARCS models (Gustafsson et al., 2008) and the PHOENIX models (Husser et al., 2013). An atmosphere model is a file with typically 72 layers. Each layer includes physical quantities such as temperature, gas and electron pressure, the optical depth, etc. The models can be calculated on the fly, but it is common practise to pre-calculate a grid of atmosphere models at certain T_{eff}, $\log g$, and [Fe /H]. A specific atmosphere model is then obtained from this grid by interpolating from nearest neighbours. The interpolation code used throughout this work includes the four nearest neighbours in the T_{eff}-space, and the two nearest neighbours in both the $\log g$- and [Fe /H]-space, in total $4 \times 2 \times 2 = 16$ atmosphere models to generate a single interpolated atmosphere model.

2.2.2 Radiative transfer code - MOOG

As mentioned above, a radiative transfer code is needed to solve the equations above. There are many different codes that does this. Here the MOOG code us used (Sneden, 1973). This code has different drivers, only some are used here.

- Derive a theoretical equivalent width (see Section 2.2.3 for details) for a given star, i.e. atmosphere model with a given set of atmospheric parameters.
- Derive line abundance from a measured equivalent width for a given model atmosphere.
- Calculate a synthetic spectrum for a given model atmosphere and atomic line list.

- Calculate the curve-of-growth for an atomic line.

There exists other drivers as well, but these are the ones used here. Some only for visualising the figures below.

2.2.3 The equivalent width

Measuring the equivalent width (EW) of spectral lines are important for some analysis of stellar spectra. The EW is a measure of the strength of the line, and dependent on the atmospheric conditions in where the spectral line is formed, such as T_{eff}, $\log g$, [Fe /H], and ξ_{micro}.

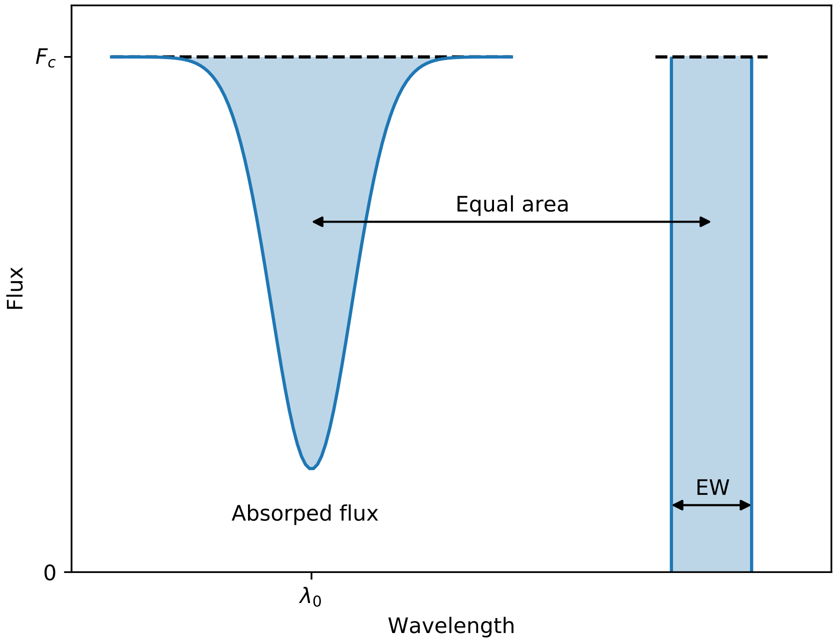

Figure 2.2: *An absorption line centred at λ_0 normalised at the flux level F_c. The area of the absorption line to the left is equal to the blue shaded area in the rectangle to the right with width EW.*

The EW is mathematically described as integrating over the entire line, and assign this area to a rectangle from 0 to the continuum flux (F_c) with the width, EW. This is illustrated in Figure 2.2 and the equation below:

$$EW = \int_0^\infty \frac{F_c - F(\lambda)}{F_c} d\lambda, \tag{2.7}$$

where λ is the wavelength. This is integral is assuming there is only one single line, hence the integral is over all wavelength. In practice the integral is calculated in small windows around a spectral line. See Section 3.3.2 for more details on how this is performed in practice. The unit of the EW is the same as the wavelength used. Throughout this thesis we will use Ångström (1Å= 0.1 nm) for the wavelength, and mÅ for the EW.

2.2.3.1 Temperature dependence

As mentioned above the EW depends on the atmospheric parameters. The dependence on T_{eff} is the strongest dependence. At low T_{eff} neutral elements, say Fe I, are the strongest lines as the number of ionized atoms are too small to contribute significantly to the EW. This is the result the Saha equation. As T_{eff} increases Fe I is converted into ionized Fe II. Slowly, as the number of Fe I decreases so does the EW, and likewise as the number of Fe II increases so does the EW. This goes on until second ionized atoms, Fe III, are formed and the same situation arise again. This is illustrated in Figure 2.3 where the EW of two iron lines, one neutral and one ionized, are plotted against T_{eff}. These two lines have similar EW in the Sun: 46.2 mÅ and 53.9 mÅ for the Fe I and Fe II line respectively.

2.2.3.2 Pressure dependence

Pressure dependence in the stellar atmosphere can be related to the gravity dependence. There are many ways to measure the pressure, and thus the gravity which is what is ultimately the goal with the measurement of $\log g$. Below are listed some of the most common methods to measure $\log g$ from spectroscopy.

- Continuum: The Balmer jump is the only continuum feature sensitive enough to estimate the $\log g$.

- Hydrogen lines: Hydrogen profiles are pressure sensitive and can therefore be used to estimate $\log g$. However, the gravity dependence rapidly diminishes for temperatures above 10 000 K.

- Other strong lines: There exists other strong lines with pressure-broadened wings such as the Ca II H and K lines. These are better for cooler stars than the hydrogen lines described above.

- Weak lines: By comparing two stages of ionization for the same element it is possible to obtain $\log g$ using weaker or modestly strong lines.

In this thesis weak lines are used to measure $\log g$. More specifically a comparison between Fe I and Fe II lines are used. For FGK stars, as the atmosphere

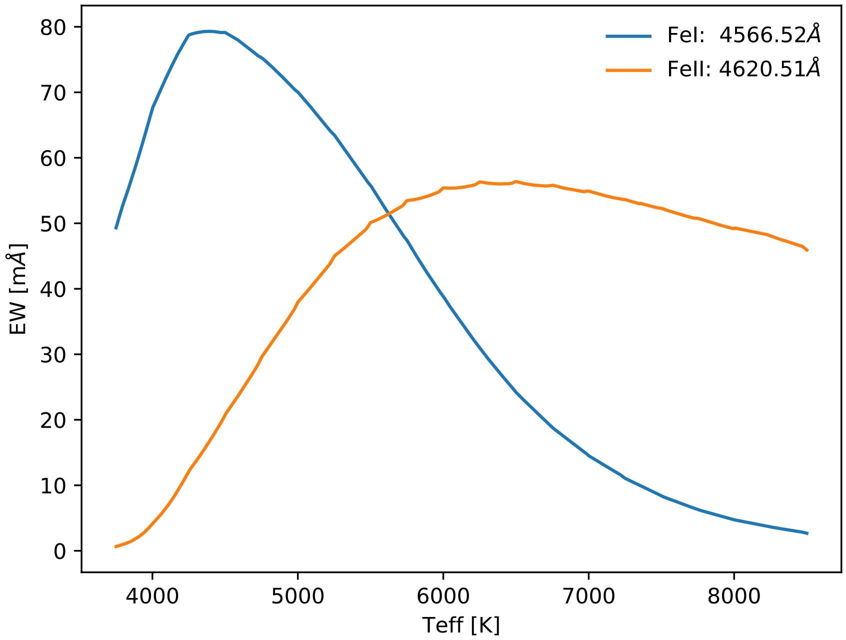

Figure 2.3: *The EW for a* Fe I *and* Fe II *line with increasing* T_{eff}. *The two lines have similar EW in the Sun and are found in the optical part of the spectrum.*

contracts (i.e. $\log g$ increases) the pressure likewise increases, which in turn means that both the gas pressure, P_g, and electron pressure, P_e, increases. Since hydrogen is the main electron contributor, but not fully ionized for these stars, the electron pressure is much smaller that the gas pressure. The gas pressure follow a simply empirical approximation with gravity:

$$P_g \approx \text{constant}\, g^{2/3}, \tag{2.8}$$

where g is the gravity. The electron pressure is given by

$$P_e \approx \text{constant}\, g^{1/3}. \tag{2.9}$$

There are three cases for which a line show dependence on gravity, when considering only weak lines:

1. A weak line formed by any ion or atom, where most of the element is in the next higher ionized state.
2. A weak line formed by any ion or atom, where most of the element is in the same ionized state.

3. A weak line formed by any ion, where most of the element is in the next lower ionized state.

Using the Saha equation for case 1, it is important to note that the number of the atoms in the highest state is roughly equal to the total number of atoms of that element, $N_{r+1} \approx N$. Hence

$$N_r \approx \text{constant } P_e \tag{2.10}$$

which means that the line absorption coefficient is

$$l_\nu \approx \text{constant } N_r \approx \text{constant } P_e. \tag{2.11}$$

The strength of a weak line, R, is proportional to the ratio of the line to the continuous absorption coefficient, κ_ν

$$R = \frac{F_c - F_\lambda}{F_c} = \text{constant } \frac{l_\nu}{\kappa_\nu}. \tag{2.12}$$

When negative hydrogen dominates κ_ν which is the case here it is proportional to the electron pressure, $\kappa_\nu \propto P_e$ which means the line strength is not proportional to to electron pressure:

$$R = \frac{l_\nu}{\kappa_\nu} \approx \text{constant}. \tag{2.13}$$

For case 2, the approach is the same, here $N_r \approx N_{r+1} \approx N = \text{constant}$. This leads to $l_\nu \approx \text{constant}$, eventually giving

$$R = \frac{l_\nu}{\kappa_\nu} \approx \frac{\text{constant}}{P_e} \approx \text{constant } g^{-1/3}. \tag{2.14}$$

Only the first two cases are relevant for solar-type stars used in this thesis, and the relation for the third case will be omitted.

In Figure 2.4 is shown how the Fe II line used previously change with $\log g$. The curve of growth is shown in the upper panel, while a synthetic spectrum for each $\log g$ is presented in the lower left panel. It is clear that the ionized line is sensitive to $\log g$ as shown in the lower right panel, where the correlation between the abundance and $\log g$ is 0.40. This is expected as can be seen in Gray (2005, Table 16.1). There is used $\delta \log A / \delta \log g$ as an indicator, and for neutral elements the correlation is much weaker. It is important to note that the correlation does change with T_{eff} and the element used.

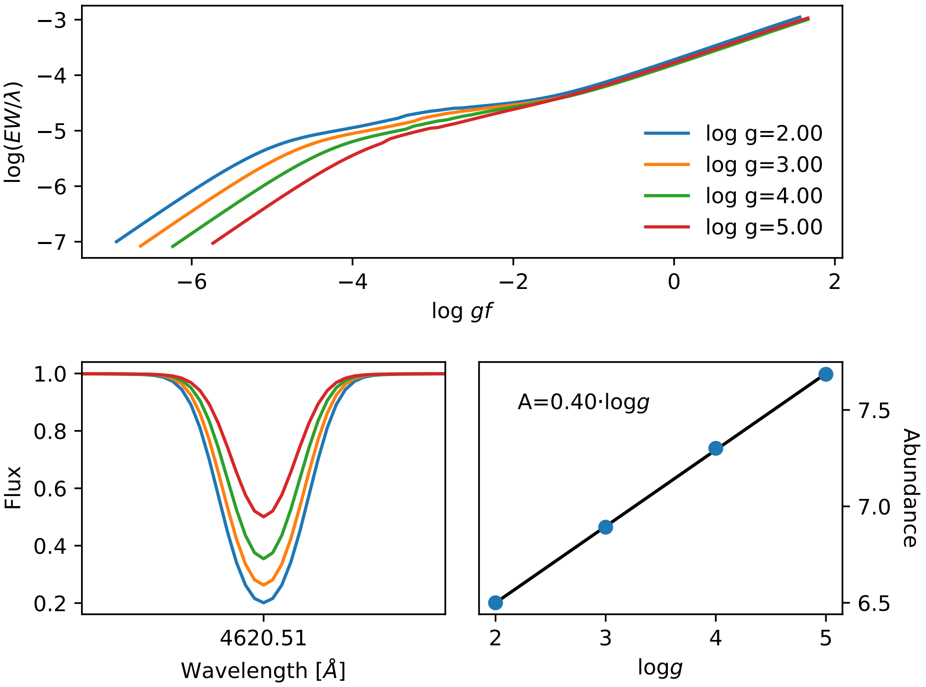

Figure 2.4: Upper panel*: Curve of growth for same* Fe II *used in Figure 2.3 for four different* $\log g$ *values. Here it is the weak lines mostly affected by the change in* $\log g$*.* Lower left panel*: Synthetic spectra of the same line. The colour scale is the same.* Lower right*: The abundance for the line at different* $\log g$*. A strong correlation (0.40) is seen.*

2.2.3.3 Abundance dependence

The abundance of a given element obviously has an effect on the EW. The more abundant an element is, the more photons can be absorbed thus increasing the EW. However, the relationship is not strictly linear. For weak lines (GIVE RANGE) EW is approximately linear with the abundance, however it reach a plateau where the core of the line saturates. In this regime the EW only increases slowly, until the absorption "spills" into the wings and the increase is again linear. However, for these strong lines the profile is no longer Gaussian. The curve of growth for the same Fe I line used in Figure 2.3 is shown in Figure 2.5. Instead of EW it is common to use the reduced EW, $\log(EW/\lambda)^1$, which we will use more later. Instead of the abundance of a line, the oscillator strength, $\log gf$, is used.

---

[1] The reduced EW is useful since it normalises Doppler-dependent phenomena, such as microturbulence and thermal broadening.

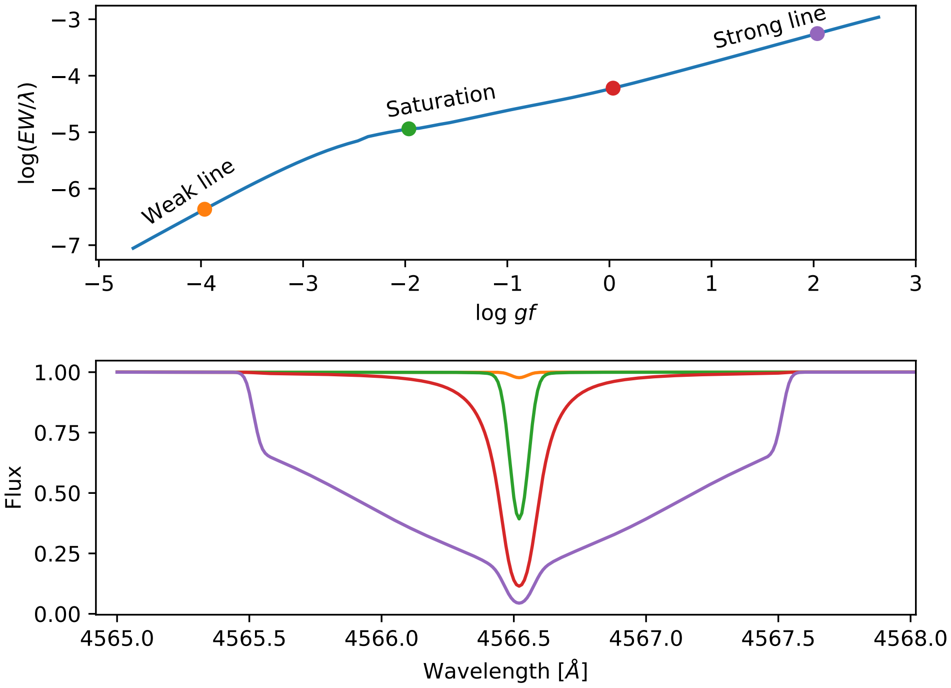

Figure 2.5: Upper panel: *Curve of growth of the same* Fe I *line as used in Figure 2.3. Four points are marked which is shown in the* lower panel *as a synthetic spectral line. The RW (proxy for EW) is clearly increasing with* $\log gf$ *(proxy for abundance).*

2.2.3.4 Microturbulence

Small-scale motion, that is motion of material at length scales small compared to the unit optical depth, are called microturbulence, ξ_{micro}. This is not to be confused with macroturbulence, which is motion of material at scales larger than the unit optical depth. The latter is associated with granulation and will not be discussed further in this thesis. ξ_{micro} comes into play when looking at the curve of growth for saturated lines (i.e. between green and red points in Figure 2.5). If no ξ_{micro} is assumed, then the measured abundance is higher than predicted by models based on thermal and damping broadening alone. In Figure 2.6 is shown three curves of growth with $\xi_{\text{micro}} = 0.5\,\text{km/s}, 2.5\,\text{km/s}, 5.0\,\text{km/s}$. As ξ_{micro} increases, so does the EW and hence the abundance.

The broadening of an absorption line measured by the shift in wavelength, $\Delta\lambda$, when ξ_{micro} is included is defined as:

$$\Delta\lambda = \frac{\lambda_0}{c}\sqrt{\frac{2kT}{m} + \xi_{\text{micro}}^2}, \tag{2.15}$$

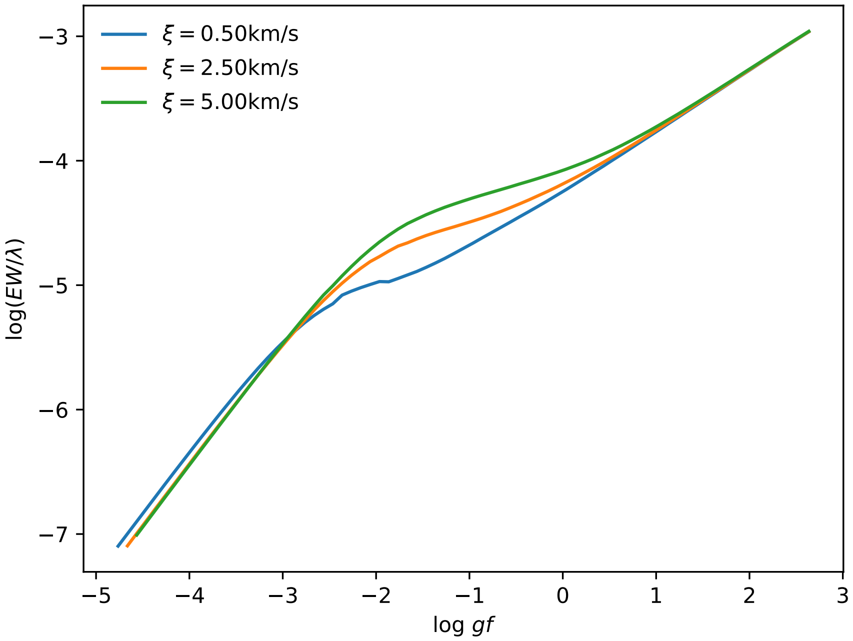

Figure 2.6: *Curve of growth for three different values of* ξ_{micro}. *The EW is increasing with increasing* ξ_{micro}.

where c is the speed of light, λ_0 is the rest wavelength of the given line, k is Boltzmann's constant, T is the temperature, and m is the mass of the atom. Setting $\xi_{\text{micro}} = 0\,\text{km/s}$, we end up with thermal broadening.

2.3 Line list and atomic data

As mentioned above, the atomic data of the absorption lines are required. These data can be found in a database such as *The Vienna Atomic Line Data Base* (VALD) (Kupka et al., 2000; Piskunov et al., 1995). For compiling a usable iron line list, all theoretical transitions in a given wavelength range are requested from VALD. In the near-infrared (NIR), YJHK bands, there are several thousands of theoretical transitions. The EWs are measured (see Section 3.3.2) for all these lines using a solar spectrum (Hinkle et al., 1995, is used here). Here there are four possible outcomes. 1) A line can not be measured and is thus discarded, 2) the EW of the line is weak (below 5 mÅ) to be reliable, 3) the EW of the line is too strong (above 150 mÅ) and the line show non-linear behaviour in the curve-of-growth (see Figure 2.5), or 4) the

EW of the line is between the two limits and is then added to the final line list.

After removing lines which EW is outside the range of EW mentioned above, it is good practise to have a visual inspection. Here one should look for severe line blending with other absorption lines which might prove problematic and unreliable measurements of the EW. If the reference spectrum used, here for the Sun, is not corrected for telluric lines, it is also a good idea to remove lines which exists amidst forest of telluric lines, as these absorption lines might fall on the telluric lines, if the star observed has a different radial velocity (RV).

When blended lines and otherwise lines which shows strange features (can be in a forest of telluric lines), the last step is to calibrate the atomic data. As mentioned above, this is done by changing the $\log gf$ value for a given line, until it has the desired determined abundance. In this case, an iron line should have the abundance of 7.47 using the values from Gonzalez and Laws (2000), when using a solar atmosphere model. There is a simple anti-correlation between the determined abundance from the measured EW and the $\log gf$, so a simple bisector minimization can be used to find the best $\log gf$. It is important to calibrate the $\log gf$ when changing the version of MOOG (or if other radiative transfer codes are used), the atmosphere model and version of those, and even the interpolation of the atmosphere models. These changes in $\log gf$ should be minor compared to the change from the VALD database and those we arrive at when calibrated for the Sun.

2.4 Spectrographs

This chapter will be focused on some of the available spectrographs for deriving stellar atmospheric parameters using the method described in Section 3.3. For this we need a spectrum of both high resolution and high signal-to-noise ratio, S/N, which combined will be called a high quality spectrum. In order to get reliable results, a spectral resolution of at least $R = \frac{\lambda}{\Delta\lambda} = 25\,000$ is needed. A $S/N \approx 100$ is at least needed to obtain the parameters. These are approximately values since it can vary across different spectral classes, e.g. it is often relatively easy to obtain parameters of a solar-twin while it gets increasingly difficult as especially T_{eff} diverges in either direction from the solar value. Naturally the higher quality the spectrum is (both resolution and S/N), the better the results will be obtained. It is common practise to increase the S/N for a spectrum by co-adding a sample of lower S/N spectra of the same star from the same spectrograph. This is often used if the star of interest is so dim that it takes several observations to reach a sufficient high S/N. Another case is when spectra have been obtained from the archive. The scientific goal can be very different, e.g. obtaining radial velocities (RV) where a much lower S/N is needed, however here numerous spectra are needed. It is common to search for exoplanets with the RV detection method, where multiple spectra are obtained, and the stellar parameters are then obtained after co-adding the multiple spectra. It is of course important to put the spectra on a common RV, usually at 0 km/s.

Spectrographs work in different wavelength regions. The most used region is the optical part of the spectrum, which is also ideal for studying FGK stars with relative low line blending and low telluric contamination. In the recent years there has been an increase of NIR spectrographs. These will mainly be used to study the distant Universe, i.e. at high red-shifts, and cool objects in our own galaxy. Especially interesting are the M stars which consist of around 70% of all stars in our galaxy (Bochanski et al., 2010). These stars are intrinsic dim because of their low T_{eff}, ranging from 2200 K to 3500 K, hence most of their light emitted will be in the NIR. It is advantageous to collect as much light as possible from these dim stars, since reaching a similar S/N in the optical would be more time expensive. The cool M stars have more molecules in the atmosphere than their hotter counterparts. This can be seen in the spectrum, where molecular lines greatly depress the continuum (and me), making EW measurements difficult. This continuum depression is much larger in the optical than the NIR, giving another motivation for studying stars in this wavelength region.

Remove stupid joke!

CHAPTER 3

DERIVING STELLAR PARAMETERS

3.1 Methods for deriving stellar atmospheric parameters

There are different methods for obtaining stellar atmospheric parameters. Here follows a short description of some of the most common methods, however the spectroscopic method will be explained in much greater detail later in this chapter.

3.1.1 InfraRed Flux Method - IRFM

The InfraRed Flux Method (IRFM) was first described by Blackwell and Shallis (1977). From IRFM it is possible to measure the stellar radius and $T_{\rm eff}$ with a measurement of the angular diameter, θ, derived from infrared photometry. $T_{\rm eff}$ is derived from the angular diameter from the simple relation

$$\sigma T_{\rm eff}^4 = \frac{4\mathcal{F}_E}{\theta^2}, \tag{3.1}$$

where $\mathcal{F}_E$ is the flux measured at Earth.

3.1.2 Photometry

3.1.3 Spectroscopy

3.2 Other stellar parameters

3.2.1 Asteroseismology

3.3 `FASMA`

In this section, the process from a spectrum to atmospheric parameters will be explained in details. There are two classic methods, synthetic fitting and curve-of-growth analysis.

The synthetic fitting method is in simple terms a comparison between the observed spectrum and a synthetic spectrum, which is either calculated on the fly like SME (Valenti and Piskunov, 1996), or using a pre-calculated grid. By analysing the χ^2 the synthetic spectrum that best match the observed spectrum can be found. This technique works for all ranges of spectral resolutions and can work for many rotational profiles as well (see e.g. Tsantaki et al., 2017). However, this method is often time-consuming compared to the curve-of-growth analysis.

Here the curve-of-growth analysis will be explained in detail. In particular Fast Analysis of Spectra Made Automatically (`FASMA`) which was developed during this thesis. `FASMA` is made of three *drivers*, 1) EW measurement driver, 2) stellar atmospheric parameters driver, and 3) abundance driver. An additional driver is under development; a synthetic fitting driver (Tsantaki et al., 2017). `FASMA` has been made available to the community via a web application[1] (Andreasen et al., 2017a).

3.3.1 Ingredients

`FASMA` is written in the Python programming language and glue together other software and models necessary for obtaining stellar atmospheric parameters from high quality spectra. These software and models are described in greater detail in the following sections. In short, the curve-of-growth analysis require measured EWs where the latest version of `ARES` is used (Sousa et al., 2015). These EWs are used to derive line abundances using model atmosphere like the ATLAS9 (Kurucz, 1993), MARCS models (Gustafsson et al., 2008), and PHOENIX models (Husser et al., 2013) to mention the most popular for this analysis. Note that the PHOENIX models are relative new and not as widely used yet. In tandem with model atmospheres a radiative transfer code is also needed. `FASMA` uses `MOOG` (Sneden, 1973) for this, however there are other codes available, e.g. . The model atmosphere usually comes in a pre-calculated grid in the $\{T_{\text{eff}}, \log g, [\text{Fe}/\text{H}]\}$ parameter space. These are interpolated in order to access the requested combination of parameters. Last, `FASMA` consist of a minimization routine which looks for the right parameters given a spectrum.

---

[1] http://www.iastro.pt/fasma/

Mention some other codes here

3.3.2 Wrapper for `ARES`

There are two ways to measure the EW of an absorption line, manual or automatic. Both of these methods are used here. There are advantages and disadvantages for both method. For the manual, an advantage is that we can inspect the lines and try to measure lines in different ways (which is useful if it is blended). We have more control over how blended lines are fitted, and which profiles are used. Disadvantages are that it is very time consuming, and it is prone to errors, as a measurement might change drastically by the eyes measuring it. Even for the same person, the measurement can change. By mentioning the advantages and disadvantages of the manual method, it should be clear that the advantages and disadvantages of the automatic method is the opposite of those. Especially the time to measure the lines are orders of magnitudes faster, which is crucial when dealing with more than a handful of spectra.

When a line is measurement by hand (manually) it is in this thesis done using the splot command in IRAF. Here the deblending mode is used whenever necessary. It is often necessary to fit one spectral lines with several Gaussians, as neighbouring lines might contaminate the line of interest slightly.

When a line is measurement automatically it is in this thesis done with `ARES` (Sousa et al., 2015, 2007). When using `ARES` it is important to use a correct value of the `rejt` parameter. This parameter is used for placing the continuum level, and is thus directly related to the final measurement EW. It is difficult to get this parameter right, however the newest version of `ARES` has the option to analyse a few absorption free regions and measure the S/N. The `rejt` is then calculated as:

$$\texttt{rejt} = 1 - \frac{1}{\text{S/N}}.$$

`ARES` is used via the first driver of `FASMA` . All the options available for `ARES` can be accessed by `FASMA` . The options are setting the spectral window, λ_{min} and λ_{max}, the RV correction to be applied or a mask to measure the RV and automatic make this correction, the minimum and maximum EW to be considered (5 mÅ and 150 mÅ respectively), the minimum distance between two consecutive lines, the smoothing applied with a *boxcar* filter before measuring the EWs. An in-depth description of these options can be found in Sousa et al. (2015, 2007).

Sometimes `ARES` crash when measuring an absorption line. The reason is not clear, however when dealing with a large amount of spectra, it is important that the analysis moves on. To deal with this problem, `FASMA` finds the last line which `ARES` tried to measure in the log file. This line is temporarily removed from the line list and `ARES` is restarted. The line list used for deriving parameters consists of numerous iron lines, thus removing one line will have a negligible effect on the final derived parameters.

3.3.3 Interpolation of atmosphere models

`FASMA` has access to both ATLAS9 models by Kurucz (1993) and MARCS models by Gustafsson et al. (2008), both are in a pre-calculated grid as described above. Let this grid be described by $\{T_{\mathrm{eff,g}},\ \log g_g,\ [\mathrm{Fe}/\mathrm{H}]_g\}$, where g is one of the grid points. Such a grid can be seen in Figure 3.1 for $[\mathrm{Fe}/\mathrm{H}] = 0.00$ in the T_{eff} range; $3000\,\mathrm{K}to10\,000\,\mathrm{K}$. For visualisation the location of the Sun is shown as well. The colour scale corresponds to the temperature in the first layer of each model atmosphere, i.e. the uppermost layer. The requested value will be $\{T_{\mathrm{eff,r}},\ \log g_r,\ [\mathrm{Fe}/\mathrm{H}]_r\}$. The task is now to find the surrounding grid points in the parameter space of the requested parameters. For $\log g$ and $[\mathrm{Fe}/\mathrm{H}]$ two neighbouring grid point are used, and for T_{eff} four surrounding grid point are used, in total $4 \times 2 \times 2 = 16$ model atmospheres for the interpolation. `FASMA` use the four surrounding grid points for T_{eff} instead of two, since the model atmosphere changes most with T_{eff}. This is common in other interpolationsas well.

Give ref here

When the 16 model atmosphere have been located, the interpolation goes through each layer of the model atmosphere, where there typical are 72 layers, and each column of which there are six. The columns are described in Section 2.2.1. The interpolation are done using the `griddata` function from `SciPy`[2]. The interpolation is linear in the parameter space. After the interpolation, the result is saved to a file in the format expected by `MOOG` .

3.3.4 Minimization

With the measured EWs for all the lines in the line list, we choose an atmosphere model to determine the abundances. If there is no prior knowledge of the star it is common simple choose a solar atmosphere model as a starting point. Next the correlation between the abundances and the reduced EWs, and the abundances and the excitation potential is calculated. If there is a correlation it means the model atmosphere used is wrong. Moreover, we also have to check if the mean abundance of Fe I and Fe II lines are equal, and last if mean abundance of the Fe I lines is equal to the input $[\mathrm{Fe}/\mathrm{H}]$ of the atmosphere model[3]. If one of these four criteria does not pass, then the

---

[2] https://scipy.org/

[3] We use Fe I instead of Fe II lines for this, since they are more numerous.

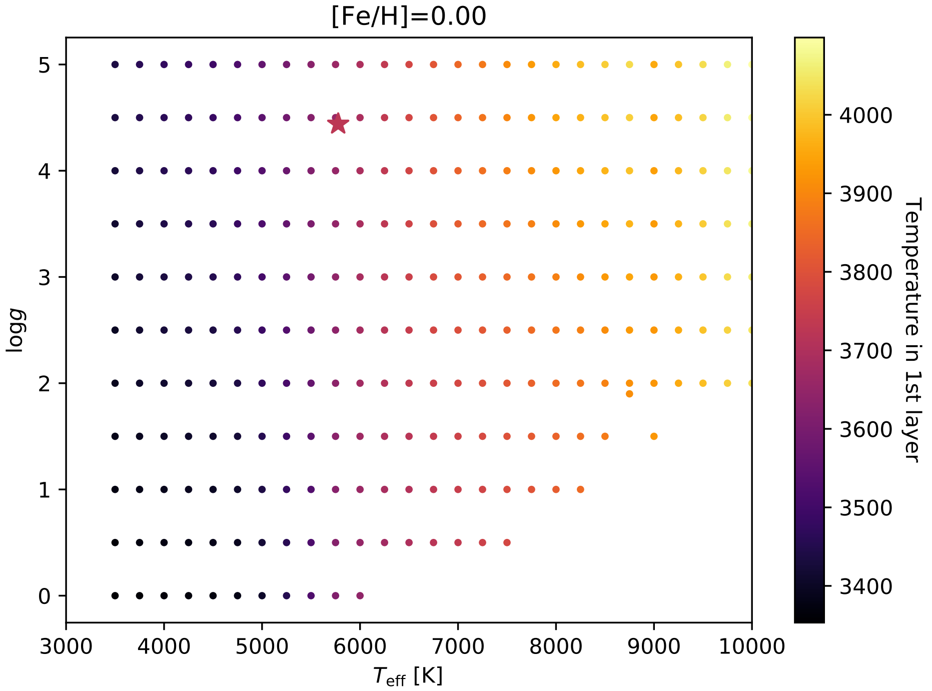

Figure 3.1: *Model atmosphere grid from Kurucz (1993) at* [Fe / H] = 0.00 *between* 3000 K *and* 10 000 K. *The grid extends to higher* $T_{\rm eff}$, *but these are not considered in this thesis.*

atmosphere model is wrong, and we have to search for a new one. A common way to do this, is by combining the indicators into a scalar value:

$$f(\{T_{\rm eff}, \log g, [Fe/H], \xi_{\rm micro}\}) = \sqrt{a_{\rm EP}^2 + a_{\rm RW}^2 + \Delta{\rm Fe}^2}, \tag{3.2}$$

where $a_{\rm EP}$ is the correlation between abundances and excitation potential, $a_{\rm RW}$ is the correlation between abundances and reduced EW, and ΔFe is the difference between the mean abundances of Fe I and Fe II. This scalar function can be minimized using standard minimization procedures as the simplex downhill among others. However, there is another approach that takes into the account the information stored in these indicators. For example, if $a_{\rm EP}$ is positive it means $T_{\rm eff}$ has to be increased by an amount correlated by the numerical value of $a_{\rm EP}$. In the same way, a non-zero $a_{\rm RW}$ means $\xi_{\rm micro}$ has to be changed, and ΔFe is an indicator for $\log g$. In the end it is a vector function being minimized which are more difficult, however we are not minimizing this using standard mathematical methods, but rather using the physical knowledge. This minimization is useless for anything else, but it is excellent for this. The vector function has the form:

$$f(\{T_{\text{eff}}, \log g, [Fe/H], \xi_{\text{micro}}\}) = \{a_{\text{EP}}, a_{\text{RW}}, \Delta\text{Fe}\,, \text{Fe}\,\textsc{i}\}. \tag{3.3}$$

The abundances of Fe I lines versus EP and RW are shown in Figure 3.2 for the planet host star HATS-1. The three rows are for three different model atmospheres. From upper to lower:

- Converged: $T_{\text{eff}} = 5959\,\text{K}$, $\log g = 4.59$, $[\text{Fe}/\text{H}] = -0.04$, and $\xi_{\text{micro}} = 1.05\,\text{km/s}$.
- Converged with 0.5 km/s added to ξ_{micro}.
- Converged with 500 K added to T_{eff}.

Left column show the abundances against the EP, and the right column is abundances against RW.

In each iteration where convergence is not reached, the input metallicity is changed to that of the mean output metallicity using the Fe I lines. The minimization is depicted in Figure 3.3. This minimization is written in the Python programming language and is also a wrapper around both `ARES` and `MOOG` . The entire package is called `FASMA` [4] (Andreasen et al., 2017a; Tsantaki et al., 2017). `FASMA` is able to fix one or all of the four atmospheric parameters, and when it reach convergence it checks if there are any outliers in the abundances. These will be removed, either all at once, all iteratively, meaning that after removing the outliers the minimization is restarted at the previous best parameters, and this process is continued until there can be removed no other outliers, or last is removing one outlier iteratively. An optical line list like the ones by Sousa et al. (2008); Tsantaki et al. (2013) have been tested thoroughly and it is safe to remove a larger amount of lines and still obtain reliable parameters. However, with a less tested line list, like the one by Andreasen et al. (2016) (and refined in Andreasen et al. (2017b)), one should remove outliers more carefully, and it is recommended that one outlier is removed iteratively.

In Figure 3.3 there is a flag with *autofixvt*. This was an option introduced since we see that some spectra does not converge, however the usual way to proceed is to fix the ξ_{micro}. This is done at the end of the minimization if the ξ_{micro} value is close to either 0km/s or 5km/s and $|a_{\text{RW}}| > 0.050$. When fixing ξ_{micro} with `FASMA` , its value is changed in each iteration following a simple empirical relation:

$$vt = \begin{cases} 6.935 \cdot 10^{-4}\ T_{\text{teff}} - 0.348 \log g - 1.437 & \text{For } \log g \geq 3.95 \\ 2.72 - 0.457 \log g + 0.072 \cdot [\text{Fe}/\text{H}] & \text{For } \log g < 3.95, \end{cases} \tag{3.4}$$

---

[4] Greek for spectrum

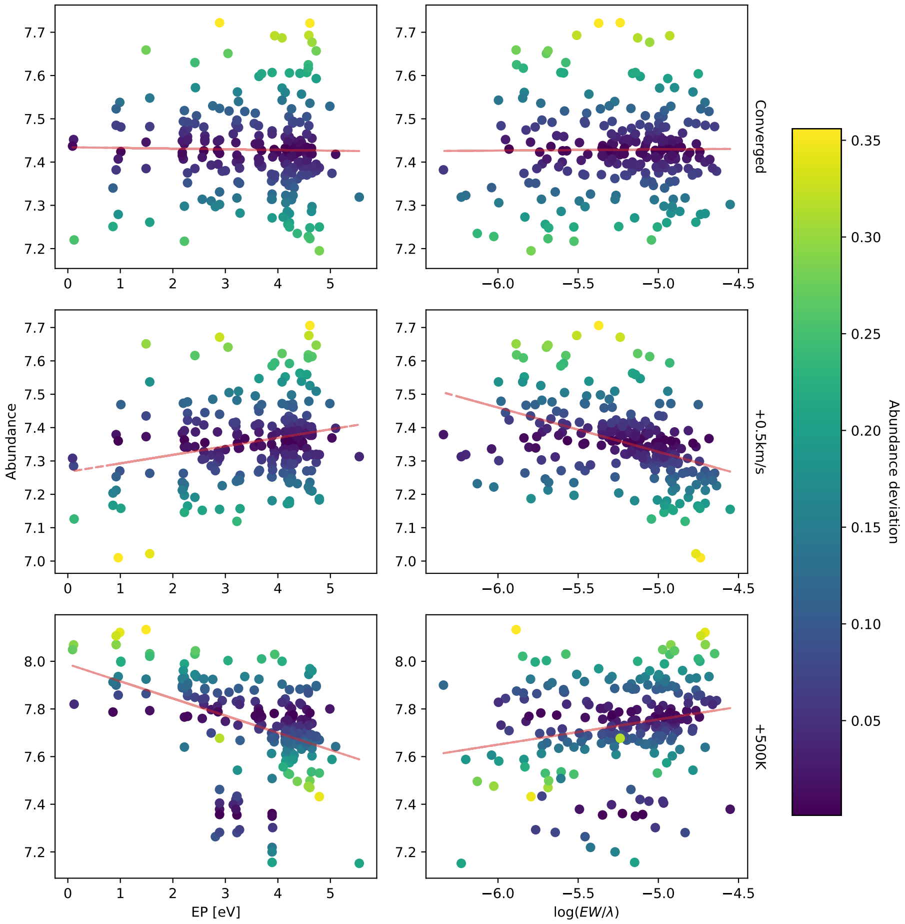

Figure 3.2: *The abundances of* Fe I *for the planet host star: HATS-1. Upper plot: Converged parameters (see text for stellar parameters for this star). Middle plot: Converged parameters with* 0.5 km/s *added to* ξ_{micro}. *Lower plot: Converged parameters with* 500 K *added to* T_{eff}.

where the first case is from Tsantaki et al. (2013) and the latter case is from Adibekyan et al. (2015).

Last there is an option, *refine*. This apply more strict criteria for the indicators to reach convergence, thus making the minimization less sensitive to the initial guess since it could otherwise reach convergence from one "side" of the parameter space. The default criteria are:

$$\begin{aligned} a_{\mathrm{EP}} &= 0.001 \\ a_{\mathrm{RW}} &= 0.003 \\ \Delta\mathrm{Fe} &= 0.001. \end{aligned}$$

The criteria for a_{RW} is not as strict as a_{EP} since this indicator can change rapidly with small changes in ξ_{micro}, thus a very strict criteria might never lead to convergence. Convergence is reached once all of the above criteria are met, and the input and output metallicity are identical. If one or more of the parameters are fixed, the corresponding criterion is simply set to 0 and effectively ignored, thus not changing the parameter.

For each iteration, the change to be applied for the atmospheric parameters are defined by adding the following:

$$T_{\mathrm{eff}} : 2000\,\mathrm{K} \cdot a_{\mathrm{EP}} \tag{3.5}$$

$$\xi_{\mathrm{micro}} : 1.5\,\mathrm{km/s} \cdot a_{\mathrm{RW}} \tag{3.6}$$

$$\log g : -\Delta\mathrm{Fe} \tag{3.7}$$

to each parameter. Note again that metallicity is simply changed to the the output metallicity of the previous iteration. These are empirical relations. Note that by changing e.g. T_{eff} not only is a_{EP} affected, but the other indicators as well. So there is a inter-dependency between the parameters, however this is ignored by `FASMA` as it is not a simple problem to solve. The stepping presented above is chosen to rapidly reach convergence, without causing problems for the inter-dependency.

3.3.5 Error estimate

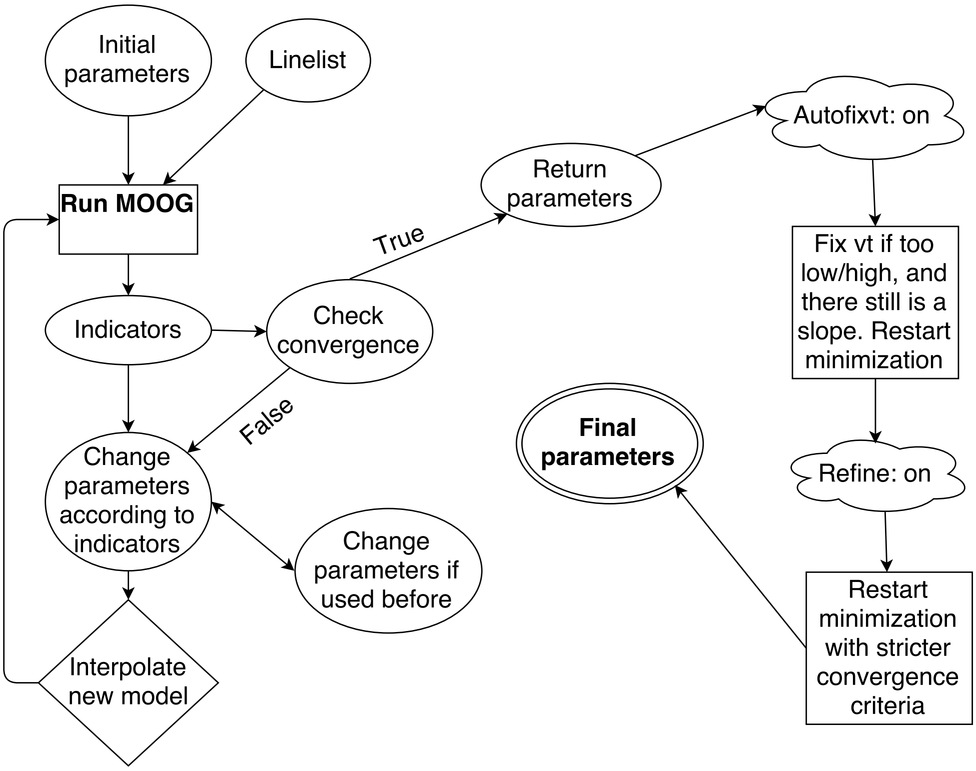
Initial parameters
Linelist
Run MOOG
Indicators
Check convergence
True
False
Return parameters
Autofixvt: on
Fix vt if too low/high, and there still is a slope. Restart minimization
Refine: on
Restart minimization with stricter convergence criteria
Final parameters
Change parameters according to indicators
Change parameters if used before
Interpolate new model

Figure 3.3: *Overview of the minimization for* `FASMA` *. Credit: Andreasen et al. (2017a).*

CHAPTER 4

RESULTS FOR FGK STARS

4.1 HD20010

4.2 Arcturus

4.3 10 Leo

4.4 Synthetic cool stars

CHAPTER 5

FUTURE WORK

BIBLIOGRAPHY

Adibekyan, V. Z., Benamati, L., Santos, N. C., Alves, S., Lovis, C., Udry, S., Israelian, G., Sousa, S. G., Tsantaki, M., Mortier, A., Sozzetti, A., and De Medeiros, J. R.: 2015, *MNRAS* **4**50, 1900

Aerts, C., Christensen-Dalsgaard, J., and Kurtz, D. W.: 2010, *Asteroseismology*, Springer-Verlag

Ammler-von Eiff, M., Santos, N. C., Sousa, S. G., Fernandes, J., Guillot, T., Israelian, G., Mayor, M., and Melo, C.: 2009, *A&A* **5**07, 523

Andreasen, D. T., Sousa, S. G., Delgado Mena, E., Santos, N. C., Tsantaki, M., Rojas-Ayala, B., and Neves, V.: 2016, *A&A* **5**85, A143

Andreasen, D. T., Sousa, S. G., Tsantaki, M., Teixeira, G. D. C., Mortier, A., Santos, N. C., Suárez-Andrés, L., Delgado Mena, E., and Ferreira, A. C. S.: 2017a, *A&A* **6**00, A69

Andreasen, D. T., Sousa, S. G., Tsantaki, M., Teixeira, G. D. C., Mortier, A., Santos, N. C., Suárez-Andrés, L., Delgado Mena, E., and Ferreira, A. C. S.: 2017b, *A&A* **5**85, A143

Artigau, É., Kouach, D., Donati, J.-F., Doyon, R., Delfosse, X., Baratchart, S., Lacombe, M., Moutou, C., Rabou, P., Parès, L. P., Micheau, Y., Thibault, S., Reshetov, V. A., Dubois, B., Hernandez, O., Vallée, P., Wang, S.-Y., Dolon, F., Pepe, F. A., Bouchy, F., Striebig, N., Hénault, F., Loop, D., Saddlemyer, L., Barrick, G., Vermeulen, T., Dupieux, M., Hébrard, G., Boisse, I., Martioli, E., Alencar, S. H. P., do Nascimento, J.-D., and Figueira, P.: 2014, in *Society of Photo-Optical Instrumentation Engineers (SPIE) Conference Series*, Vol. 9147 of *Society of Photo-Optical Instrumentation Engineers (SPIE) Conference Series*, p. 15

Baraffe, I., Homeier, D., Allard, F., and Chabrier, G.: 2015, *A&A* **5**77, A42

Bensby, T., Feltzing, S., and Oey, M. S.: 2014, *A&A* **5**62, A71

Blackwell, D. E. and Shallis, M. J.: 1977, *MNRAS* **1**80, 177

Bochanski, J. J., Hawley, S. L., Covey, K. R., West, A. A., Reid, I. N., Golimowski, D. A., and Ivezić, Ž.: 2010, *AJ* **1**39, 2679

Boyajian, T. S., von Braun, K., van Belle, G., McAlister, H. A., ten Brummelaar, T. A., Kane, S. R., Muirhead, P. S., Jones, J., White, R., Schaefer, G., Ciardi, D., Henry, T., López-Morales, M., Ridgway, S., Gies, D., Jao, W.-C., Rojas-Ayala, B., Parks, J. R., Sturmann, L., Sturmann, J., Turner, N. H., Farrington, C., Goldfinger, P. J., and Berger, D. H.: 2012, *ApJ* **7**57, 112

Casagrande, L., Ramírez, I., Meléndez, J., Bessell, M., and Asplund, M.: 2010, *A&A* **5**12, A54

Conod, U., Blind, N., Wildi, F., and Pepe, F.: 2016, in *Society of Photo-Optical Instrumentation Engineers (SPIE) Conference Series*, Vol. 9909 of *Proceedings of the SPIE*, p. 990941

Delfosse, X., Donati, J.-F., Kouach, D., Hébrard, G., Doyon, R., Artigau, E., Bouchy, F., Boisse, I., Brun, A. S., Hennebelle, P., Widemann, T., Bouvier, J., Bonfils, X., Morin, J., Moutou, C., Pepe, F., Udry, S., do Nascimento, J.-D., Alencar, S. H. P., Castilho, B. V., Martioli, E., Wang, S. Y., Figueira, P., and Santos, N. C.: 2013, in L. Cambresy, F. Martins, E. Nuss, and A. Palacios (eds.), *SF2A-2013: Proceedings of the Annual meeting of the French Society of Astronomy and Astrophysics*, pp 497–508

Dotter, A., Chaboyer, B., Jevremović, D., Kostov, V., Baron, E., and Ferguson, J. W.: 2008, *ApJS* **1**78, 89

Follert, R., Dorn, R. J., Oliva, E., Lizon, J. L., Hatzes, A., Piskunov, N., Reiners, A., Seemann, U., Stempels, E., Heiter, U., Marquart, T., Lockhart, M., Anglada-Escude, G., Löwinger, T., Baade, D., Grunhut, J., Bristow, P., Klein, B., Jung, Y., Ives, D. J., Kerber, F., Pozna, E., Paufique, J., Kaeufl, H. U., Origlia, L., Valenti, E., Gojak, D., Hilker, M., Pasquini, L., Smette, A., and Smoker, J.: 2014, in *Society of Photo-Optical Instrumentation Engineers (SPIE) Conference Series*, Vol. 9147 of *Society of Photo-Optical Instrumentation Engineers (SPIE) Conference Series*, p. 19

Girardi, L., Bressan, A., Bertelli, G., and Chiosi, C.: 2000, *A&A Supp.* **1**41, 371

Gonzalez, G. and Laws, C.: 2000, *AJ* **1**19, 390

Gray, D. F.: 2005, *The Observation and Analysis of Stellar Photospheres, 3rd ed.*

Gustafsson, B., Edvardsson, B., Eriksson, K., Jørgensen, U. G., Nordlund, Å., and Plez, B.: 2008, *A&A* **4**86, 951

Hinkle, K. H., Wallace, L., and Livingston, W.: 1995, in A. J. Sauval, R. Blomme, and N. Grevesse (eds.), *Laboratory and Astronomical High Resolution Spectra*, Vol. 81 of *Astronomical Society of the Pacific Conference Series*, p. 66

Husser, T.-O., Wende-von Berg, S., Dreizler, S., Homeier, D., Reiners, A., Barman, T., and Hauschildt, P. H.: 2013, *A&A* **5**53, A6

Kippenhahn, R. and Weigert, A.: 1994, *Stellar Structure and Evolution*, Springer-Verlag

Kjeldsen, H. and Bedding, T. R.: 1995, *A&A* **2**93, 87

Kotani, T., Tamura, M., Suto, H., Nishikawa, J., Sato, B., Aoki, W., Usuda, T., Kurokawa, T., Kashiwagi, K., Nishiyama, S., Ikeda, Y., Hall, D. B., Hodapp, K. W., Hashimoto, J., Morino, J.-I., Okuyama, Y., Tanaka, Y., Suzuki, S., Inoue, S., Kwon, J., Suenaga, T., Oh, D., Baba, H., Narita, N., Kokubo, E., Hayano, Y., Izumiura, H., Kambe, E., Kudo, T., Kusakabe, N., Ikoma, M., Hori, Y., Omiya, M., Genda, H., Fukui, A., Fujii, Y., Guyon, O., Harakawa, H., Hayashi, M., Hidai, M., Hirano, T., Kuzuhara, M., Machida, M., Matsuo, T., Nagata, T., Onuki, H., Ogihara, M., Takami, H., Takato, N., Takahashi, Y. H., Tachinami, C., Terada, H., Kawahara, H., and Yamamuro, T.: 2014, in *Society of Photo-Optical Instrumentation Engineers (SPIE) Conference Series*, Vol. 9147 of *Society of Photo-Optical Instrumentation Engineers (SPIE) Conference Series*, p. 14

Kupka, F. G., Ryabchikova, T. A., Piskunov, N. E., Stempels, H. C., and Weiss, W. W.: 2000, *Baltic Astronomy* **9**, 590

Kurucz, R.: 1993, *ATLAS9 Stellar Atmosphere Programs and 2 km/s grid. Kurucz CD-ROM No. 13. Cambridge, Mass.: Smithsonian Astrophysical Observatory, 1993.* 13

Lebzelter, T., Heiter, U., Abia, C., Eriksson, K., Ireland, M., Neilson, H., Nowotny, W., Maldonado, J., Merle, T., Peterson, R., Plez, B., Short, C. I., Wahlgren, G. M., Worley, C., Aringer, B., Bladh, S., de Laverny, P., Goswami, A., Mora, A., Norris, R. P., Recio-Blanco, A., Scholz, M., Thévenin, F., Tsuji, T., Kordopatis, G., Montesinos, B., and Wing, R. F.: 2012, *A&A* **5**47, A108

Lindgren, S., Heiter, U., and Seifahrt, A.: 2016, *A&A* **5**86, A100

Meléndez, J. and Barbuy, B.: 1999, *ApJS* **1**24, 527

Mucciarelli, A., Pancino, E., Lovisi, L., Ferraro, F. R., and Lapenna, E.: 2013, *ApJ* **7**66, 78

Önehag, A., Heiter, U., Gustafsson, B., Piskunov, N., Plez, B., and Reiners, A.: 2012, *A&A* **5**42, A33

Origlia, L., Oliva, E., Baffa, C., Falcini, G., Giani, E., Massi, F., Montegriffo, P., Sanna, N., Scuderi, S., Sozzi, M., Tozzi, A., Carleo, I., Gratton, R., Ghinassi, F., and Lodi, M.: 2014, in *Society of Photo-Optical Instrumentation Engineers (SPIE) Conference Series*, Vol. 9147 of *Society of Photo-Optical Instrumentation Engineers (SPIE) Conference Series*, p. 1

Piskunov, N. E., Kupka, F., Ryabchikova, T. A., Weiss, W. W., and Jeffery, C. S.: 1995, *A&A Supp.* **1**12, 525

Quirrenbach, A., Amado, P. J., Caballero, J. A., Mundt, R., Reiners, A., Ribas, I., Seifert, W., Abril, M., Aceituno, J., Alonso-Floriano, F. J., Ammler-von Eiff, M., Antona Jiménez, R., Anwand-Heerwart, H., Azzaro, M., Bauer, F., Barrado, D., Becerril, S., Béjar, V. J. S., Benítez, D., Berdiñas, Z. M., Cárdenas, M. C., Casal, E., Claret, A., Colomé, J., Cortés-Contreras, M., Czesla, S., Doellinger, M., Dreizler, S., Feiz, C., Fernández, M., Galadí, D., Gálvez-Ortiz, M. C., García-Piquer, A., García-Vargas, M. L., Garrido, R., Gesa, L., Gómez Galera, V., González Álvarez, E., González Hernández, J. I., Grözinger, U., Guàrdia, J., Guenther, E. W., de Guindos, E., Gutiérrez-Soto, J., Hagen, H.-J., Hatzes, A. P., Hauschildt, P. H., Helmling, J., Henning, T., Hermann, D., Hernández Castaño, L., Herrero, E., Hidalgo, D., Holgado, G., Huber, A., Huber, K. F., Jeffers, S., Joergens, V., de Juan, E., Kehr, M., Klein, R., Kürster, M., Lamert, A., Lalitha, S., Laun, W., Lemke, U., Lenzen, R., López del Fresno, M., López Martí, B., López-Santiago, J., Mall, U., Mandel, H., Martín, E. L., Martín-Ruiz, S., Martínez-Rodríguez, H., Marvin, C. J., Mathar, R. J., Mirabet, E., Montes, D., Morales Muñoz, R., Moya, A., Naranjo, V., Ofir, A., Oreiro, R., Pallé, E., Panduro, J., Passegger, V.-M., Pérez-Calpena, A., Pérez Medialdea, D., Perger, M., Pluto, M., Ramón, A., Rebolo, R., Redondo, P., Reffert, S., Reinhardt, S., Rhode, P., Rix, H.-W., Rodler, F., Rodríguez, E., Rodríguez-López, C., Rodríguez-Pérez, E., Rohloff, R.-R., Rosich, A., Sánchez-Blanco, E., Sánchez Carrasco, M. A., Sanz-Forcada, J., Sarmiento, L. F., Schäfer, S., Schiller, J., Schmidt, C., Schmitt, J. H. M. M., Solano, E., Stahl, O., Storz, C., Stürmer, J., Suárez, J. C., Ulbrich, R. G., Veredas, G., Wagner, K., Winkler, J., Zapatero Osorio, M. R., Zechmeister, M., Abellán de Paco, F. J., Anglada-Escudé, G., del Burgo, C., Klutsch, A., Lizon, J. L., López-Morales, M., Morales, J. C., Perryman, M. A. C., Tulloch, S. M., and Xu, W.: 2014, in *Society of Photo-Optical Instrumentation Engineers (SPIE) Conference Series*, Vol. 9147 of *Society of Photo-Optical Instrumentation Engineers (SPIE) Conference Series*, p. 1

Ramírez, I. and Meléndez, J.: 2005, *ApJ* **6**26, 446

Rayner, J., Bond, T., Bonnet, M., Jaffe, D., Muller, G., and Tokunaga, A.: 2012, in *Ground-based and Airborne Instrumentation for Astronomy IV*, Vol. 8446 of *Proceedings of the SPIE*, p. 84462C

Rayner, J., Tokunaga, A., Jaffe, D., Bonnet, M., Ching, G., Connelley, M., Kokubun, D., Lockhart, C., and Warmbier, E.: 2016, in *Society of Photo-Optical Instrumentation Engineers (SPIE) Conference Series*, Vol. 9908 of *Proceedings of the SPIE*, p. 990884

Recio-Blanco, A., Bijaoui, A., and de Laverny, P.: 2006, *MNRAS* **3**70, 141

Santos, N. C., Sousa, S. G., Mortier, A., Neves, V., Adibekyan, V., Tsantaki, M., Delgado Mena, E., Bonfils, X., Israelian, G., Mayor, M., and Udry, S.: 2013, *A&A* **5**56, A150

Sneden, C. A.: 1973, *Ph.D. thesis*, THE UNIVERSITY OF TEXAS AT AUSTIN.

Sousa, S. G., Santos, N. C., Adibekyan, V., Delgado-Mena, E., and Israelian, G.: 2015, *A&A* **5**77, A67

Sousa, S. G., Santos, N. C., Israelian, G., Mayor, M., and Monteiro, M. J. P. F. G.: 2007, *A&A* **4**69, 783

Sousa, S. G., Santos, N. C., Mayor, M., Udry, S., Casagrande, L., Israelian, G., Pepe, F., Queloz, D., and Monteiro, M. J. P. F. G.: 2008, *A&A* **4**87, 373

Torres, G., Andersen, J., and Giménez, A.: 2010, *Astronomy and Astrophysics Reviews* **1**8, 67

Torres, G., Fischer, D. A., Sozzetti, A., Buchhave, L. A., Winn, J. N., Holman, M. J., and Carter, J. A.: 2012, *ApJ* **7**57, 161

Torres, G., Winn, J. N., and Holman, M. J.: 2008, *ApJ* **6**77, 1324

Tsantaki, M., Andreasen, D. T., Teixeira, G. D. C., Sousa, S. G., Santos, N. C., Delgado-Mena, E., and Bruzual, G.: 2017, *MNRAS* **5**55, A150

Tsantaki, M., Sousa, S. G., Adibekyan, V. Z., Santos, N. C., Mortier, A., and Israelian, G.: 2013, *A&A* **5**55, A150

Tsantaki, M., Sousa, S. G., Santos, N. C., Montalto, M., Delgado-Mena, E., Mortier, A., Adibekyan, V., and Israelian, G.: 2014, *A&A* **5**70, A80

Valenti, J. A. and Fischer, D. A.: 2005, *ApJS* **1**59, 141

Valenti, J. A. and Piskunov, N.: 1996, *A&A Supp.* **1**18, 595